International Journal of Mechanical Sciences 249 (2023) 108246

Contents lists available at ScienceDirect

International Journal of Mechanical Sciences

journal homepage: www.elsevier.com/locate/ijmecsci

An analytical self-consistent model for the adhesion of Gibson solid

Yudong Zhu [a], Zhijun Zheng [a,*], Chenguang Huang [b,c], Jilin Yu [a]

[a] CAS Key Laboratory of Mechanical Behavior and Design of Materials, Department of Modern Mechanics, University of Science and Technology of China, Hefei, 230027, China

[b] Key Laboratory for Mechanics in Fluid Solid Coupling Systems, Institute of Mechanics, Chinese Academy of Sciences, Beijing, 100190, China

[c] Hefei Institutes of Physical Science, Chinese Academy of Sciences, Hefei, 230031, China

ARTICLE INFO

Keywords:
Adhesive contact
Gibson solid
Toy model
Folding deformation
Asymptotic solution

ABSTRACT

A full self-consistent model (FSCM) for the adhesive contact between an axisymmetric rigid punch and a Gibson solid (an incompressible, linear graded elastic material) is established, which gives a self-consistent relation between the surface gap and interaction. Power-law shaped indenters and the Lennard–Jones interaction law are studied as representative cases, and the self-consistent equation is expressed in a dimensionless form with two independent parameters, namely the shape index and the Tabor number. The self-consistent equation for Gibson solid is a higher order polynomial equation with respect to the surface gap, which differs from the nonlinear integral equation for power-law graded elastic material. By taking the surface gap as the independent variable instead of the radius, the self-consistent equation is solved explicitly, which gives the first explicit form of the solution to an FSCM. When the Tabor number exceeds a critical value, jump-in instability and adhesion hysteresis occur, and the folding phenomenon that the Gibson solid surface is flipped and folded along the radial direction is observed. The critical Tabor number is determined in an explicit form and it is found to be independent of the surface index. The extended Maugis–Dugdale (M–D) model for Gibson solid is invalid when the Tabor number is large enough and the extended Johnson–Kendall–Roberts (JKR) model does not present the soft limit, due to their assumption of simple contact. An asymptotic solution is derived for the soft limit of the FSCM, which gives a power-law asymptotic relation between the dimensionless pull-off force and the Tabor number. This study provides a self-consistent toy model for the adhesive contact of Gibson solid and may deepen the understanding on the adhesion of graded materials.

1. Introduction

Graded materials and structures exist widely in the natural biological adhesion systems, which may achieve strong, stable, and robust adhesion [1–3]. It is a great challenge to consider the effect of gradient in adhesive contact theory, and some progress has only been made in the recent decade [4–12]. Among various graded materials, the most typical one is the incompressible material with Young's modulus increasing linearly with depth, which is well known as a Gibson solid [13]. The study on the adhesion behavior of Gibson solid is fundamental and important, and may offer some basic understanding and new insights of general graded materials. Recently, Zhu et al. [14] developed a self-consistent adhesive contact model for power-law graded materials, which provides an alternative analytical framework for the adhesion of graded materials, but its form is implicit and the numerical calculation method may fail for Gibson solid. Therefore, this study makes a further attempt on understanding the adhesion of Gibson solid.

Gibson solid first attracted interest in the field of geology and was introduced to study the settlement of foundations on soils [13]. Although it may be too ideal to simplify actual solid material to be an incompressible and linearly graded elastic material, some basic understanding on the mechanical properties of graded materials can be obtained by using Gibson solid as a toy model. An interesting property of Gibson solid is that the surface local deformation is directly proportional to the local pressure [13]. This property is also valid for anisotropic incompressible linearly graded materials [15,16], but does not hold when considering the effect of finite depth [17] and Poisson's ratio [18]. A comprehensive analysis on the mechanical response of Gibson solid under line/point loading was presented by Calladine and Greenwood [19]. The study on Gibson solid opens the prelude to the contact problems of general graded materials. For example, Booker et al. [20,21] derived the displacement solutions of power-law graded material under various loadings, and Giannakopoulos and Suresh [22,23] presented the Hertz solutions to the contact problems of power-/exponential-law graded materials.

The above research laid a solid foundation for developing the adhesion models of graded materials. Yao and Gao [24,25] conducted

* Corresponding author.
E-mail address: zjzheng@ustc.edu.cn (Z.J. Zheng).

https://doi.org/10.1016/j.ijmecsci.2023.108246
Received 10 January 2023; Received in revised form 18 February 2023; Accepted 18 February 2023
Available online 27 February 2023

studies on the adhesion of Gibson solid through an interfacial crack model and found that this material can achieve flaw-tolerant adhesion, i.e., the adhesion stress uniformly reaches the theoretical strength at the pull-off point and is independent of the crack size. Several adhesive contact models of Gibson solid were established by deriving the limit solutions of power-law graded material [5,9,10]. For example, Chen et al. [5] extended the Johnson–Kendall–Roberts (JKR) model [26] to power-law graded material, and found that the pull-off force for the contact between a sphere and Gibson solid is $2\pi R\Delta\gamma$ (R the sphere radius and $\Delta\gamma$ the interface energy). Jin et al. [9] obtained the JKR–DMT transition of power-law graded material by extending the double-Hertz model [27], and concluded that the pull-off force $-P_c$ between a sphere and Gibson solid is identical to $2\pi R\Delta\gamma$ and its dimentionless form $-P_c/(\pi R\Delta\gamma)$ is independent of the transition parameter, i.e., the Tabor number. It was found that this understanding is valid only for the paraboloidal-shaped punch by using a generalized Maugis–Dugdale (M–D) model [10]. In the extended double-Hertz and M–D models of Gibson solid, the Tabor number is limited from 0 to 1 [9,10]. For small Tabor numbers, the double-Hertz-type and M–D-type models both reduce to the Derjaguin–Muller–Toporov (DMT) model [9,10,27,28], and the DMT pull-off force is independent of the gradient parameter [10,14]. However, it is expected that the Tabor number can be very large for strong adhesion (e.g., large interface energy) and soft materials (small Young's modulus). This indicates that the previous solution on the adhesion of Gibson solid is incomplete, and a full understanding may need more accurate models.

In the framework of continuum mechanics, the full self-consistent model (FSCM) [29–31] is the most accurate adhesion model and it may provide an opportunity to overcome the above limitation. The FSCM adopts a self-consistent relation between the surface interaction and the surface deformation through a specific force law, and does not impose any additional restrictions on the surface deformation. In comparison, the JKR-type and M–D-type models adopt the simple contact assumption (the surface gap within a central zone is single-valued and equals to zero), and the DMT-type model adopts the Hertzian shape assumption (the surface contour remains Hertzian and is not affected by adhesion). The FSCM has successfully characterized adhesion properties between homogeneous solids from rigid to soft contact [32–34]. Previous studies on the FSCM mainly focused on different surface shapes [35–38]. Zhu et al. [14] made the first attempt to establish an FSCM for the adhesive contact of nonhomogeneous materials, and successfully used it to validate and improve the corresponding M–D model. However, the numerical calculation of the self-consistent nonlinear integral equation becomes intractable when it approaches the Gibson limit, where a step function is involved. In addition, the FSCMs for homogeneous and power-law graded material in all previous studies have no explicit solution and requires a complex control method and a numerical iterative method to solve the self-consistent relation [14,32,33,35–38], which greatly limits the application of FSCM and is the main reason why FSCM has not received enough attention, compared with the JKR-type and the M–D-type models.

This study aims to develop an FSCM for the adhesive contact between a rigid punch and a Gibson solid, and to make the first attempt to derive an analytical solution of FSCM. The present work is a necessary supplement to the recent study on the adhesion of power-law graded material [14], and may be regarded as a fundamental toy model for the adhesive contact of graded materials. Theoretical modeling and solving strategies are presented in Section 2. In Section 3, the adhesion behavior between a power-law-shaped punch and Gibson solid is analyzed, and the extended JKR and M–D models are verified by the present model. Conclusions are given in Section 4.

2. Theory

In this section, an FSCM for the adhesive contact of Gibson solid is established. The self-consistent equation is expressed in an explicit form by exchanging variables, and a solution strategy is presented.

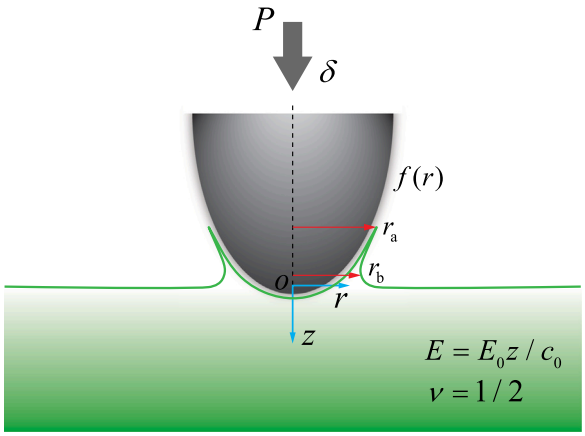

Fig. 1. Schematic of the adhesive contact between an axisymmetric rigid punch and an incompressible, linear graded half-space (Gibson solid). During contact, adhesion necking may occur. In an adhesion neck, r_a represents the neck outer radius and r_b represents the neck inner radius.

2.1. A full self-consistent model for the adhesion of gibson solid

The adhesive contact problem between an axisymmetric rigid punch and a Gibson-type half-space is studied, as shown in Fig. 1. For the Gibson solid, the Poisson's ratio ν is $1/2$ (incompressible material) and its Young's modulus E increases linearly with depth z according to [13]

$$E(z) = E_0 \frac{z}{c_0}, \tag{1}$$

where E_0 is a reference modulus and c_0 is the characteristic depth. The surface shape of the rigid punch is described by $f(r)$, and the surface gap between the two objects is given by

$$H(r) = -\delta + f(r) + w(r), \tag{2}$$

where δ is the relative displacement of distant points in the two solids and $w(r)$ is the surface deformation of Gibson solid. For a given surface interaction $p(r)$, the surface deformation $w(r)$ can be calculated by using the fundamental solution of contact mechanics.

Here, we adopted the Derjaguin approximation [14,32,38–41] to describe the surface interaction. In this approximation, the force between curved and inclined surfaces is assumed to be identical to that between plane and parallel surfaces, which is a function with respect to the local surface gap, i.e.,

$$p(r) = p_s(H(r)). \tag{3}$$

The total force is given by

$$P = \int_0^\infty p_s(H(r)) 2\pi r \, \mathrm{d}r. \tag{4}$$

For an FSCM, the relation between the surface interaction and the surface deformation is self-consistent [29–31]. The surface interaction $p(r)$ is determined by the local surface gap $H(r)$ through Eq. (3). Correspondingly, the surface deformation $w(r)$ is determined by $p(r)$, and then affects $H(r)$ through Eq. (2). We propose two approaches to establish the self-consistent relation for the adhesive contact of Gibson solid.

Recently, Zhu et al. [14] have studied the adhesion of power-law graded elastic materials with a constant Poisson's ratio ν and a Young's modulus E, described by

$$E = E_0 (z/c_0)^k, \quad 0 \le k < 1, \tag{5}$$

where k is the gradient exponent. It is noted that the region of k in contact problems can be $-1 < k < 1$ [42–46], and the absolute value

of k can be larger than 1 for the Poisson's ratio $\nu = 1/2$ [46,47]. In this study, we focus on the adhesion of incompressible, linear graded elastic material, i.e., $k = 1$ and $\nu = 1/2$.

Using the Derjaguin approximation and an analytical surface displacement solution of a half-space under a ring loading [21], Zhu et al. [14] obtained the full self-consistent equation for power-law graded materials. By applying the Riemann–Stieltjes integral method and the properties of Gauss's hypergeometric function, the full self-consistent equation is rewritten in a form without integral singularity [14], i.e.,

$$H(r) = -\delta + f(r) + \frac{2bc_0^k r^{1-k}}{E^*(1-k)} \int_{t=0}^{t=\infty} p_s(H(t))\mathrm{d}\Psi_k(t/r) + \frac{2bc_0^k}{E^*(1-k)} \int_{t=0}^{t=\infty} p_s(H(t))\mathrm{d}t^{1-k}, \tag{6}$$

where $E^* = E_0/(1-\nu^2)$ and parameter b is given by

$$b = \frac{2^{k+1}(k+2)\,q\sin(q\pi/2)}{k(k+1)\,\mathrm{B}(k/2,1/2)}\mathrm{B}\left(\frac{3+k+q}{2},\frac{3+k-q}{2}\right),$$
$$q = \sqrt{(1+k)\left(1-\frac{k\nu}{1-\nu}\right)}, \tag{7}$$

with $\mathrm{B}(\cdot)$ denoting the Euler's beta function. The function $\Psi_k(s)$ is defined as [14]

$$\Psi_k(s) = \frac{1}{2(1+s)^k}\left[(s-1)\,{}_2\mathrm{F}_1\left(\frac{k+1}{2},\frac{1}{2};1;\frac{4s}{(1+s)^2}\right) + (1+s)\,{}_2\mathrm{F}_1\left(\frac{k-1}{2},\frac{1}{2};1;\frac{4s}{(1+s)^2}\right)\right] - s^{1-k}, \tag{8}$$

where ${}_2\mathrm{F}_1(\cdot)$ is the Gauss's hypergeometric function. When $k \to 1$, we have $b/(1-k) \to 1$ for $\nu = 1/2$, and $b/(1-k) \to \infty$ for $\nu \neq 1/2$. Thus, for $k = 1$, the value of Poisson's ratio must be 1/2 (Gibson solid), and the function $\Psi_k(s)$ approaches a step function, written as

$$\lim_{k\to 1}\Psi_k(s) = \theta(s) = \begin{cases} 0, & s > 1, \\ -1, & s < 1. \end{cases} \tag{9}$$

Hence, Eq. (6) can be reduced to

$$H(r) = -\delta + f(r) + \frac{3c_0}{2E_0}\int_{t=0}^{t=\infty} p_s(H(t))\mathrm{d}\theta(t/r). \tag{10}$$

The step function $\theta(s)$ is discontinuous at $s = 1$ and it brings difficulties to the numerical integration of Eq. (10). Fortunately, it is known that the derivative of the step function $\theta(s)$ is the Dirac delta function $\delta_\mathrm{D}(s-1)$, which is defined by $\delta_\mathrm{D}(x) = 0$ for $x \neq 0$ and $\int_{-\infty}^{\infty}\delta_\mathrm{D}(x)\mathrm{d}x = 1$. Consequently, Eq. (10) can be rewritten as

$$H(r) = -\delta + f(r) + \frac{3c_0}{2E_0}\int_0^{\infty} p_s(H(sr))\delta_\mathrm{D}(s-1)\mathrm{d}s. \tag{11}$$

By applying the sifting property of the delta function, the full self-consistent equation for Gibson solid can be derived as

$$H(r) = -\delta + f(r) + \frac{3c_0}{2E_0}p_s(H(r)). \tag{12}$$

In fact, by using a special property of Gibson solid, the full self-consistent equation can be derived in an alternative approach. The normal deformation behavior of the Gibson-type half-space acts as a Winkler foundation, i.e., the normal surface deformation $w(r)$ is directly proportional to the local pressure $p(r)$ [13,19]

$$w(r) = \frac{p(r)}{k_s}, \tag{13}$$

where k_s is the parameter of substrate reaction. This parameter is independent of the shape and size of the loading zone, and equal to twice the increase rate of shear modulus G with depth, i.e., $k_s = 2G/z$ [13]. For elastic materials, the relation between the Young's modulus and the shear modulus is $E = 2G(1+\nu)$, and then for Gibson solid ($\nu = 1/2$), we have $E = 3G$. By combining these relations with Eq. (1), the parameter k_s can be given by

$$k_s = \frac{2E_0}{3c_0}. \tag{14}$$

Substituting Eqs. (3), (13) and (14) into Eq. (2) also leads to Eq. (12). This confirms that the FSCM for the adhesion of Gibson solid is a limit case of that for the adhesion of power-law graded elastic materials [14]. It is common to consider the surface modulus to be zero in the adhesion of graded materials for analytical tractability [4–12,14,48], and this limitation may be overcome through numerical or asymptotic methods [49,50].

It should be noted that the full self-consistent equations for homogeneous material [32] and power-law graded material [14] are both nonlinear integral equations. The surface gap at each radius is coupled with the surface gaps at other positions in these integral equations, which need numerical iterative methods to solve [14,32]. However, for Gibson solid, the full self-consistent equation, Eq. (12), shows that the surface gaps are decoupled from each other and any surface gap depends only on a local radius. Therefore, the solving method of Eq. (12) can be much simpler, as presented in Section 2.3.

2.2. Nondimensionalization

The full self-consistent equation can be solved for given surface shape $f(r)$ and surface interaction $p_s(H)$. Here, we considered the power-law surface shapes described by [11,51]

$$f(r) = \frac{r^n}{nQ}, \tag{15}$$

where n is the shape index and Q is the shape parameter. For $n = 1$, $Q = \tan\phi$, and for $n \neq 1$, $Q = R^{n-1}$. In particular, $n = 1$ represents a cone with ϕ being the semiangle, and $n = 2$ represents a sphere with R being the radius. The 9–3 Lennard–Jones (L–J) force law is taken as an example to describe the surface interaction [9,10,14,32], i.e.,

$$p_s(H) = \frac{8\Delta\gamma}{3z_0}\left[\left(\frac{H}{z_0}+1\right)^{-9} - \left(\frac{H}{z_0}+1\right)^{-3}\right], \tag{16}$$

where $\Delta\gamma$ is the interface energy per unit area and z_0 is the characteristic distance of the surface interaction range. The interval of H/z_0 is $(-1,\infty)$. When $H/z_0 < 0$, the surface pressure is positive (corresponding to compressive stress), and two surfaces are in contact.

By introducing the following dimensionless parameters

$$\bar{H} = \frac{H}{z_0}, \quad \bar{\delta} = \frac{\delta}{z_0}, \quad \bar{r} = \frac{r}{(Qz_0)^{1/n}}, \tag{17}$$

the surface shape and interaction can be rewritten in a dimensionless form as

$$\bar{f}(\bar{r}) \equiv \frac{f(r)}{z_0} = \frac{\bar{r}^n}{n}, \tag{18}$$

$$\bar{p}_s(\bar{H}) \equiv \frac{p_s(H)}{\Delta\gamma/z_0} = \frac{8}{3}\left[(\bar{H}+1)^{-9} - (\bar{H}+1)^{-3}\right], \tag{19}$$

respectively. Then, the full self-consistent equation (Eq. (12)) can be rewritten as

$$\bar{H} - \frac{16}{3}\mu^2\left[(\bar{H}+1)^{-9} - (\bar{H}+1)^{-3}\right] + \bar{\delta} = \bar{f}(\bar{r}), \tag{20}$$

where μ is the generalized Tabor number for Gibson solid, defined as

$$\mu = \sqrt{\frac{3c_0\Delta\gamma}{4E_0z_0^2}}. \tag{21}$$

The definition of the Tabor number for Gibson solid coincides with that for power-law graded materials in the limit of $k = 1$ and $\nu = 1/2$ [9,10,14]. The Tabor number for Gibson solid is independent of shape parameters, and the full self-consistent equation (Eq. (20)) is controlled by two independent dimensionless parameters, i.e., n and μ. The self-consistent equation (Eq. (20)) for the present problem is a higher order

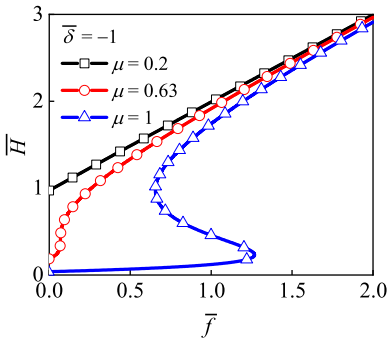

Fig. 2. The relation between the dimensionless surface gap $\bar{H}$ and the dimensionless surface shape function $\bar{f}$ for three special values of Tabor numbers μ with $\bar{\delta} = -1$. $\bar{H}$ is single-valued with respect to $\bar{f}$ for a small Tabor number and may be multivalued for a large Tabor number. The critical Tabor number is about 0.63.

polynomial equation with respect to $\bar{H}$, which is quite different from the nonlinear integral equations of homogeneous material [32] and power-law graded material [14]. The dimensionless total force is given by

$$\bar{P} \equiv \frac{P}{\pi Q^{2/n} \Delta\gamma z_0^{2/n-1}} = 2\int_0^{\infty} \bar{p}_s(\bar{H}(\bar{r}))\bar{r}\mathrm{d}\bar{r}. \tag{22}$$

2.3. Solution strategies

In a usual solution strategy, the radius $\bar{r}$ is chosen as the independent variable for the self-consistent equation. For given $\bar{r}$, n, μ, and $\bar{\delta}$, the surface gap $\bar{H}$ can be calculated numerically from Eq. (20) through some standard methods, such as the dichotomy method and the secant method. After $\bar{H}(\bar{r})$ is determined, the dimensionless total load $\bar{P}$ can be obtained from Eqs. (19) and (22). By changing $\bar{\delta}$ from a large value (say 10) to a small value (say −10), all the equilibrium states ($\bar{P}$ vs. $\bar{\delta}$) can be obtained from Eqs. (20) and (22). However, Eq. (20) is a higher order polynomial equation of $\bar{H}$ and it has multiple roots when the Tabor number is large, which makes it difficult to select proper solutions during the calculation procedure.

Taking $\bar{r}$ as the independent variable is inappropriate when the Tabor number is large. Note that $\bar{f}(\bar{r})$ of the power-law surface shapes increases monotonously for $\bar{r} > 0$, and choosing $\bar{r}$ as the independent variable is equivalent to making $\bar{f}$ as the independent variable. The variation of $\bar{H}$ with $\bar{f}$ is plotted for three representative values of μ and $\bar{\delta} = -1$, as shown in Fig. 2. The value of $\bar{\delta}$ does not affect the trend of the curve, and only makes the curves shift in the horizontal direction. When the Tabor number is small (say $\mu = 0.2$), $\bar{H}$ is single-valued with respect to $\bar{f}$ (or $\bar{r}$). But, when the Tabor number is large (say $\mu = 1$), $\bar{H}$ may have multiple values with respect to $\bar{f}$ (or $\bar{r}$), which causes difficulties in the root selection. The critical Tabor number μ_c for this transition is about 0.63, which is analyzed below.

The necessary mathematical condition for $\bar{H}$ to appear multivalued is

$$\frac{\mathrm{d}\bar{H}}{\mathrm{d}\bar{r}} \to \infty \quad \text{or} \quad \frac{\mathrm{d}\bar{r}}{\mathrm{d}\bar{H}} = 0 \tag{23}$$

at some radii. Differentiating both sides of Eq. (20) with respect to $\bar{H}$ yields

$$1 - 16\mu^2\left[(\bar{H}+1)^{-4} - 3(\bar{H}+1)^{-10}\right] = \frac{\mathrm{d}\bar{f}(\bar{r})}{\mathrm{d}\bar{r}}\frac{\mathrm{d}\bar{r}}{\mathrm{d}\bar{H}}. \tag{24}$$

Notice that the value of $\mathrm{d}\bar{f}(\bar{r})/\mathrm{d}\bar{r}$ is finite, and then Eqs. (23) and (24) leads to

$$1 - 16\mu^2\left[(\bar{H}+1)^{-4} - 3(\bar{H}+1)^{-10}\right] = 0, \tag{25}$$

or

$$\mu = \frac{1}{4}\left[(\bar{H}+1)^{-4} - 3(\bar{H}+1)^{-10}\right]^{-1/2}, \tag{26}$$

which has a minimum μ_c at $\bar{H} = (15/2)^{1/6} - 1 \approx 0.40$, i.e.,

$$\mu_c = \frac{5}{4\sqrt[6]{60}} \approx 0.63. \tag{27}$$

It is very interesting to find that the inverse relation ($\bar{f}$ vs. $\bar{H}$, or $\bar{r}$ vs. $\bar{H}$) is always single-valued for all the cases studied, as shown in Fig. 2. Therefore, we can choose $\bar{H}$ instead of $\bar{r}$ to be the independent variable in the numerical calculation. For power-law surface shapes, Eq. (20) can be rewritten as

$$\bar{r}(\bar{H}) = n^{1/n}\left\{\bar{\delta} + \bar{H} - \frac{16}{3}\mu^2\left[(\bar{H}+1)^{-9} - (\bar{H}+1)^{-3}\right]\right\}^{1/n}. \tag{28}$$

It can be found from Eq. (28) that the full self-consistent equation is in an explicit form if $\bar{H}$ is taken as the independent variable. The surface central gap control method [14] is adopted in this study to obtain all equilibrium states. At the position $\bar{r} = 0$, Eq. (28) gives

$$\bar{\delta} = -\bar{H}_0 + \frac{16}{3}\mu^2\left[(\bar{H}_0+1)^{-9} - (\bar{H}_0+1)^{-3}\right], \tag{29}$$

where $\bar{H}_0$ is the surface gap at $\bar{r} = 0$. Then, Eq. (22) can be rewritten as

$$\bar{P} = 2\int_{\bar{H}=\bar{H}_0}^{\bar{H}=\infty} \bar{p}_s(\bar{H})\,\bar{r}(\bar{H})\,\mathrm{d}\,\bar{r}(\bar{H}), \tag{30}$$

which can be calculated through numerical integration. The preset interval of $\bar{H}$ is $(\bar{H}_0, \infty)$, but it is noted that if $\bar{f} < 0$, the value of $\bar{r}$ is unreasonable. Hence, the independent variable $\bar{H}$ should be restricted to a reasonable interval, as discussed below.

In the surface central gap control method, $\bar{H}_0$ varies from a large value (say 10) to a small value (say −0.1). From Eqs. (20) and (29), we have

$$\bar{f}(\bar{r}(\bar{H})) = \bar{H} - \bar{H}_0 - \frac{16}{3}\mu^2\left[(\bar{H}+1)^{-9} - (\bar{H}+1)^{-3} - (\bar{H}_0+1)^{-9} + (\bar{H}_0+1)^{-3}\right], \quad \bar{H} \geq \bar{H}_0. \tag{31}$$

For $\mu \leq 0.63$, $\bar{f}$ increases monotonously with the increase of $\bar{H}$, so $\bar{f} \geq 0$ and $\bar{r} \geq 0$ for any value of $\bar{H} \geq \bar{H}_0$. But for $\mu > 0.63$, $\bar{f}$ is nonmonotonic with respect to $\bar{H}$ and there are some local extreme points in an $\bar{f}$ vs. $\bar{H}$ curve. As an example of $\mu = 1$, a local maximum (denoted as point A) and a local minimum (denoted as point B) can be observed in Fig. 3. The points with the same $\bar{f}$ values of A and B are denoted as A′ and B′, respectively. For different values of $\bar{H}_0$, the effective integral interval of $\bar{H}$ is analyzed here. When $\bar{H}_0 \geq \bar{H}_B$ or $\bar{H}_0 \leq \bar{H}_{B'}$, we always have $\bar{f} \geq 0$ for $\bar{H} \geq \bar{H}_0$, as illustrated in Figs. 3(a) and 3(d). When $\bar{H}_A \leq \bar{H}_0 < \bar{H}_B$, it is found that the condition $\bar{f} > 0$ satisfies only for $\bar{H} > \bar{H}_1$ with $\bar{H}_1$ being the corresponding largest root to $\bar{f} = 0$, as shown in Fig. 3(b). When $\bar{H}_{B'} < \bar{H}_0 < \bar{H}_A$, the condition $\bar{f} > 0$ is hold for $\bar{H}_0 < \bar{H} < \bar{H}_1$ and $\bar{H} > \bar{H}_2$, with $\bar{H}_1$ and $\bar{H}_2$ being the two larger roots corresponding to $\bar{f} = 0$, as shown in Fig. 3(c). Therefore, the attainable interval of $\bar{H}$ can be determined for any case. Actually, in the numerical integral of Eq. (30), the surface gap $\bar{H}$ can take a continuous change from $\bar{H}_0$ to a large enough value, with a careful treatment of $\bar{f} < 0$, i.e., if $\bar{f} < 0$, one can take $\bar{f} = 0$ and $\bar{r} = 0$, which does not contribute to the integral in Eq. (30).

3. Results and discussion

In this section, the effect of the Tabor number and the shape index on the adhesive contact behavior of Gibson solid is analyzed. The adhesion hysteresis and the surface deformation mode are discussed and a related critical condition is derived. The FSCM is used to validate the M–D-*n*-G and JKR-*n*-G models, and an asymptotic solution for the soft limit of Gibson solid adhesion is obtained based on our FSCM.

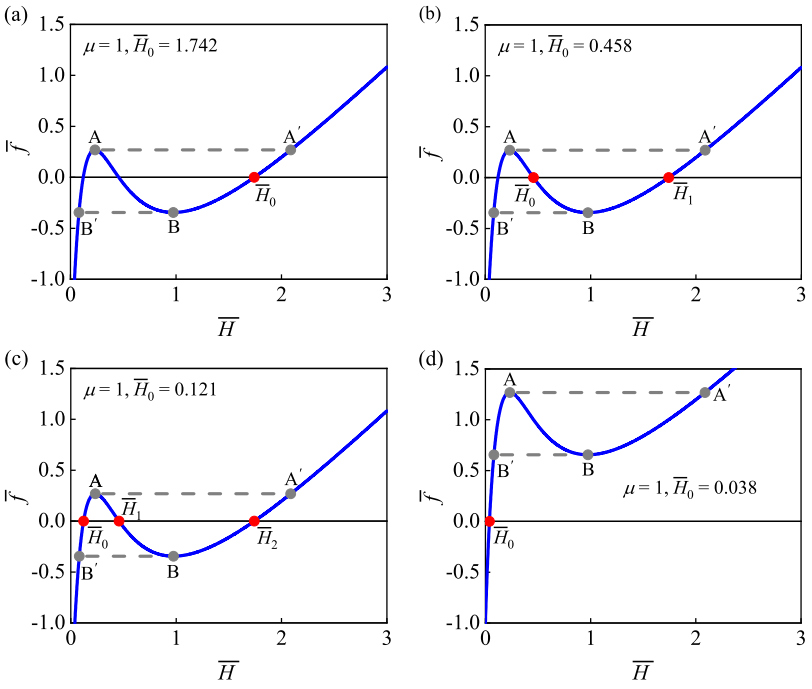

Fig. 3. Variation of the dimensionless surface shape function $\bar{f}$ with the dimensionless surface gap $\bar{H}$ for $\mu = 1$ and four representative positions of the dimensionless surface central gap: (a) $\bar{H}_0 = 1.742$, (b) $\bar{H}_0 = 0.458$, (c) $\bar{H}_0 = 0.121$, and (d) $\bar{H}_0 = 0.038$. $\bar{H}_0$, $\bar{H}_1$ and $\bar{H}_2$ are three roots of $\bar{f} = 0$. The local maximum/minimum of $\bar{f}$ is denoted as point A/B, and the points with the same $\bar{f}$ values of A and B are denoted as A′ and B′, respectively.

3.1. Adhesion features at small/large Tabor numbers

The force–displacement curves for $n = 2$ and $\mu = 0.2$ and 2 are studied as representative cases, as shown in Fig. 4. According to the magnitude of the force or the characteristics of the displacement, some representative points are marked on the curves. The force–displacement curve is single-valued at small Tabor numbers, as shown in Fig. 4(a) for a case of $n = 2$ and $\mu = 0.2$. If the displacement control method is adopted, the loading path is A–B–C–D and the unloading path is the opposite one D–C–B–A. But, the full force–displacement curve is bifurcated at large Tabor numbers, thus the adhesion hysteresis phenomenon appears if the displacement control method is adopted, as elaborated in Fig. 4(b) for a case of $n = 2$ and $\mu = 2$. In this case, the loading path is A–B–B′–C–D and there is an unstable jumping-in process (B → B′). The unloading path is D–C–B′–M–A and there is no jumping instability during detachment. This interesting adhesion behavior of Gibson solid has also been observed for materials with $\nu = 1/2$ and $k > 1$ [47]. During a complete loading–unloading cycle, some mechanical energy is dissipated due to the unstable jumping process (namely the hysteresis energy loss), which is represented by the shadow area (ABB′A) in Fig. 4(b).

The surface deformation and pressure distribution along the radius direction for some representative points (marked in Fig. 4) on the force–displacement curves are plotted in Fig. 5. For the cases considered, the surface deformation at point A is almost zero, because the distance between the punch and the half-space is large and the surface interaction is very weak. The surface of the half-space is piled up during loading from point A to point B, corresponding to tensile deformation. In the loading path, the maximum value of tensile deformation increases until a critical value is reached, as shown in Figs. 5(a) and 5(b). This is because the deformation of the Gibson solid is proportional to the local pressure and the surface tensile pressure has a maximum (namely the theoretical strength), as presented in Figs. 5(c) and 5(d). The theoretical strength can be obtained by calculating the extremum of Eq. (16) as $\sigma_{\text{th}} \approx 1.026\Delta\gamma/z_0$. By using Eqs. (13), (14) and (21), the dimensionless maximum tensile deformation is given by $-\bar{w}_{\max} \approx 2.052\mu^2$. For the small Tabor number, the surface deformation and pressure are single-valued and change continuously during the loading/unloading process, as illustrated in Figs. 5(a) and 5(c). For a large Tabor number (say $\mu = 2$), the surface deformation and pressure change suddenly at the jumping-in position (B → B′), as shown in Figs. 5(b) and 5(d). It is interesting to find that the surface of Gibson solid is flipped and folded along the radial direction (corresponding to an adhesion neck), and the surface deformation and pressure are multivalued for some intervals of radius, which is named as a folding deformation mode. This folding phenomenon appears at point B′ with $\bar{r} = 0$ being the fold position. From point B′ to point D, the fold position moves outward. Experimental tests on the adhesive contact of Gibson solid have not been reported in the literature, but the folding deformation has been observed in some experiments on the adhesion of homogeneous soft materials [52–54].

The folding deformation mode has not been predicted by the JKR-/M–D-type models for the adhesion of Gibson solid [5,9,10], see Section 3.4 for further discussion. In the FSCM for the adhesion of power-law graded materials ($0 < k < 1$) [14] and homogeneous materials [32,35], the folding deformation mode is not observed either. This is because, for a general material, the self-consistent relation in the FSCM usually contains a nonlinear integral, which characterizes the mutual inhibition of deformation by surface interactions at different radii. In addition, the full self-consistent equation for a general material is in an implicit form, and the surface gap H cannot be separated as an independent variable like the Gibson toy model in this study. Thus, we can only choose the radius r as the independent variable and H as the dependent variable, i.e., H is single-valued with respect to r and it is impossible to predict the folding deformation.

Two parameters are introduced to characterize the shape of the adhesion neck, i.e., the neck outer radius r_{a} and the neck inner radius r_{b}, as illustrated in Fig. 1. The surface gaps corresponding to r_{a} and r_{b} are denoted as H_{a} and H_{b}, respectively. Their dimensionless forms are $\bar{r}_{\text{a}} = r_{\text{a}}/(Rz_0)^{1/2}$, $\bar{r}_{\text{b}} = r_{\text{b}}/(Rz_0)^{1/2}$, $\bar{H}_{\text{a}} = H_{\text{a}}/z_0$ and, $\bar{H}_{\text{b}} = H_{\text{b}}/z_0$. From the definition of the neck radius, Eq. (23) is valid for $\bar{r} = \bar{r}_{\text{a}}$ and $\bar{r} = \bar{r}_{\text{b}}$. Thus, $\bar{H}_{\text{a}}$ and $\bar{H}_{\text{b}}$ can be determined by solving Eq. (25) for a given Tabor number, and are independent of the shape index n and

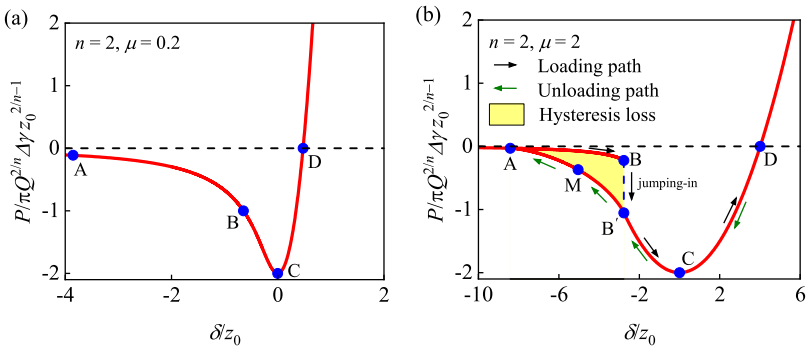

Fig. 4. The force–displacement curves for (a) $n = 2, \mu = 0.2$ and (b) $n = 2, \mu = 2$. For $\mu = 0.2$, the loading path is A–B–C–D and the unloading path is the opposite one D–C–B–A. For $\mu = 2$, the loading path is A–B–B′–C–D and the unloading path is D–C–B′–M–A. Adhesion hysteresis is observed in (b) and the shadow area (ABB′A) represents the hysteresis energy.

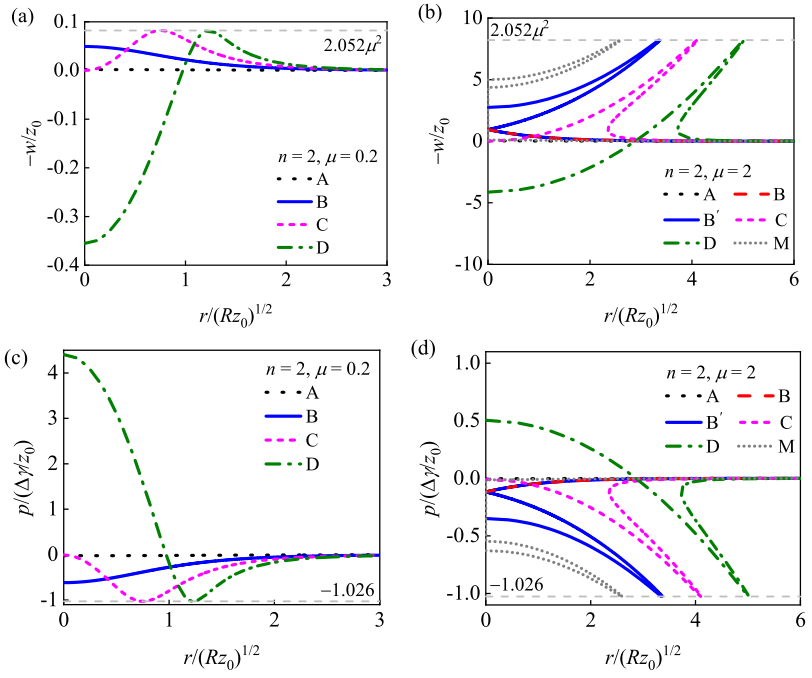

Fig. 5. The surface deformation of some representative points on the force–displacement curves for (a) $\mu = 0.2$ and (b) $\mu = 2$, and the corresponding pressure distribution for (c) $\mu = 0.2$ and (d) $\mu = 2$. Points A, B, B′, C, D, and M are marked in Fig. 4. A folding deformation mode appears for $\mu = 2$, and the surface deformation in (b) and pressure distribution in (d) are both multivalued.

the displacement $\bar{\delta}$. After $\bar{H}_a$ and $\bar{H}_b$ are determined, $\bar{r}_a$ and $\bar{r}_b$ can be obtained by using Eq. (20) for given values of μ, n, and $\bar{\delta}$. The effect of the Tabor number μ on $\bar{H}_a$ and $\bar{H}_b$ is studied in Fig. 6(a). For $\mu < 0.63$, $\bar{H}_a$ and $\bar{H}_b$ do not have corresponding values, because the adhesion neck does not appear. As the Tabor number increases, $\bar{H}_a$ decreases monotonously and approaches to a constant value, and $\bar{H}_b$ increases monotonously. The asymptotic behavior of $\bar{H}_a$ and $\bar{H}_b$ can be studied by using a principal balance method. It can be seen from the exact results in Fig. 6(a) that $\bar{H}_a + 1$ has the order of 1 and $\bar{H}_b + 1 \to \infty$ as $\mu \to \infty$. Thus, the two dominant terms in Eq. (25) when $\bar{H}$ is around $\bar{H}_a$ are $-16\mu^2(\bar{H}+1)^{-4}$ and $48\mu^2(\bar{H}+1)^{-10}$. By balancing the dominant terms of Eq. (25), the asymptotic solution of $\bar{H}_a$ as $\mu \to \infty$ is derived as

$$\bar{H}_a \sim 3^{1/6} - 1 \approx 0.201, \qquad \mu \to \infty. \tag{32}$$

When $\bar{H}$ is around $\bar{H}_b$, the two dominant terms in Eq. (25) are 1 and $-16\mu^2(\bar{H}+1)^{-4}$ as $\mu \to \infty$. The asymptotic solution of $\bar{H}_b$ is given by

$$\bar{H}_b \sim 2\sqrt{\mu} - 1, \quad \mu \to \infty. \tag{33}$$

The asymptotic solutions of $\bar{H}_a$ and $\bar{H}_b$ almost coincide with the exact results for $\mu > 1.5$, as shown in Fig. 6(a). The dependency of $\bar{r}_a$ and $\bar{r}_b$ on the displacement $\bar{\delta}$ during the loading/unloading process is analyzed for $n = 2$ and $\mu = 2$, as shown in Fig. 6(b). The points A, M, B′, C, and D are corresponding to those marked in Fig. 4(b). In the loading process, $\bar{r}_a$ and $\bar{r}_b$ increase monotonously from point B′(the appearance point of the folding deformation), which corresponds to an outward-moving adhesion neck. In the unloading process, $\bar{r}_a$ and $\bar{r}_b$ decrease monotonously along the path D–C–B′–M–A, and the adhesion neck moves inward. During detachment, $\bar{r}_b$ vanishes at the parts B′–M–A, and then $\bar{r}_a$ vanishes if the displacement continues to decrease after point A.

3.2. Effect of the shape index and the Tabor number

The effect of the Tabor number on the full force–displacement curves is studied for some special values of shape index n, as shown in Fig. 7. A bifurcated curve is observed for $\mu = 1$ and 2 in all the studied cases for the shape index. For $n < 2$, the displacement corresponding to the pull-off point i.e., the point associated with the pull-off force on

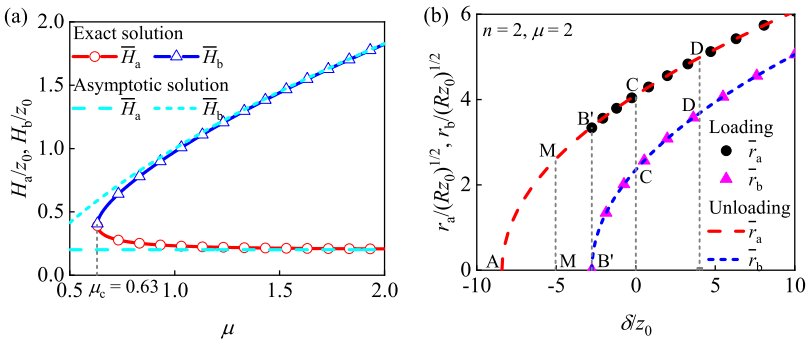

Fig. 6. (a) Effect of the Tabor number μ on the surface gaps $\bar{H}_a$ and $\bar{H}_b$ corresponding to the adhesion neck outer radius $\bar{r}_a$ and inner radius $\bar{r}_b$, respectively. The critical Tabor number for $\bar{H}_a$ and $\bar{H}_b$ to have values is $\mu_c = 0.63$. Asymmetric solutions of $\bar{H}_a$ and $\bar{H}_b$ are plotted in dashed lines. (b) Dependency of $\bar{r}_a$ and $\bar{r}_b$ on the displacement $\bar{\delta}$ during the loading/unloading process for $n = 2$ and $\mu = 2$. The loading path is B′–C–D and the unloading path is D–C–B′–M–A, where points A, B, B′, C, D, and M are marked in Fig. 4(b).

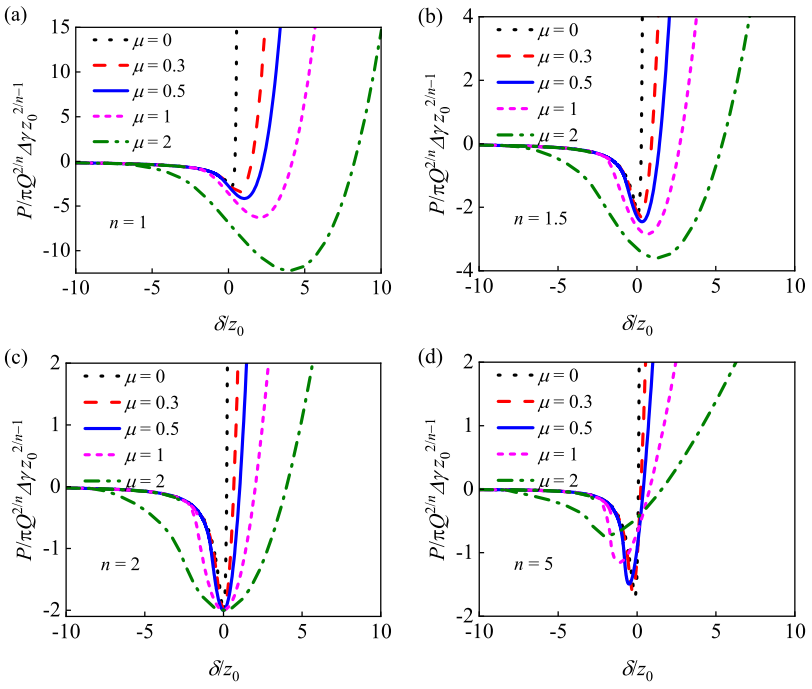

Fig. 7. Effect of the Tabor number μ on the force–displacement curves with some specific values of the shape index: (a) $n = 1$, (b) $n = 1.5$, (c) $n = 2$, and (d) $n = 5$. The representative values of μ are 0, 0.3, 0.5, 1, and 2.

the force–displacement curve is positive and increases with the increase of the Tabor number, as shown in Figs. 7(a) and 7(b). For $n > 2$, the displacement corresponding to the pull-off point is negative and decreases with the increase of the Tabor number, as shown in Fig. 7(d). For $n = 2$, the pull-off point occurs at $\bar{\delta} = 0$ and the corresponding dimensionless pull-off force (i.e., the maximum value of $-\bar{P}$) is 2, as shown in Fig. 7(c).

It is interesting to find that the dimensionless pull-off displacement and pull-off force do not change with the Tabor number for $n = 2$. Actually, the total force for $n = 2$ can be derived explicitly. Substituting Eq. (28) with $n = 2$ into Eq. (30) leads to

$$\bar{P} = -\frac{8}{3\left(\bar{H}_0+1\right)^2} + \frac{2}{3\left(\bar{H}_0+1\right)^8} + \frac{128\mu^2}{9\left(\bar{H}_0+1\right)^6} - \frac{256\mu^2}{9\left(\bar{H}_0+1\right)^{12}} + \frac{128\mu^2}{9\left(\bar{H}_0+1\right)^{18}}. \tag{34}$$

The relation between $\bar{\delta}$ and $\bar{H}_0$ is given by Eq. (29). It is easy to find that $\bar{H}_0 = 0$ gives

$$\frac{\mathrm{d}\bar{P}}{\mathrm{d}\bar{H}_0} = 0, \quad \frac{\mathrm{d}^2\bar{P}}{\mathrm{d}\bar{H}_0^2} > 0. \tag{35}$$

Consequently, the pull-off point emerges at $\bar{H}_0 = 0$. Substituting $\bar{H}_0 = 0$ into Eqs. (29) and (34) yields the displacement and force at the pull-off point, i.e.,

$$\bar{\delta}_c = 0, \quad -\bar{P}_c = 2, \tag{36}$$

which are indeed independent of the Tabor number. This finding is consistent with that predicted by the generalized double-Hertz and M–D models for Gibson solid [9,10].

The effect of the Tabor number on the pull-off force is analyzed for some cases of the shape index n, as shown in Fig. 8(a). As the Tabor number increases, the dimensionless pull-off force increases monotonically for the cases of $n = 1$ and 1.5, and decreases monotonically for the case of $n = 5$. The dimensionless pull-off forces of the Bradley-n model [51] and the JKR model for Gibson solid (denoted as the JKR-n-G model) [5,10] are also plotted for comparison, which are given by

$$-\bar{P}_c^{\text{Bradley-}n} \equiv \frac{-P_c^{\text{Bradley-}n}}{\pi Q^{2/n}\Delta\gamma z_0^{2/n-1}} = \frac{32n^{2/n}}{9n-2}\mathrm{B}\left(3-\frac{2}{n},\frac{2}{n}\right)\left[168\mathrm{B}\left(4-\frac{2}{n},6\right)\right]^{(3n-2)/(6n)} \tag{37}$$

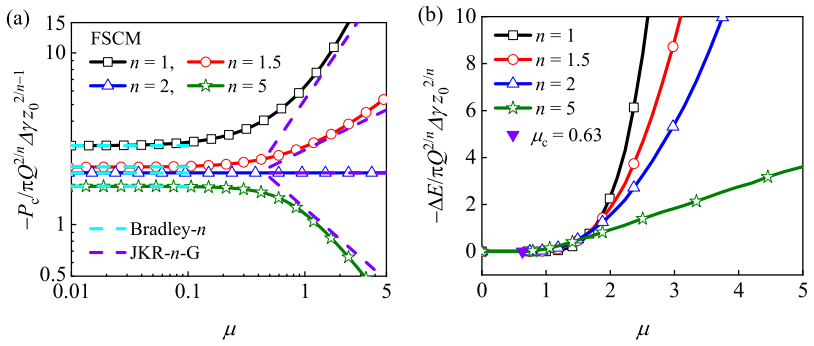

Fig. 8. Effect of the Tabor number μ on (a) the pull-off force and (b) the apparent hysteresis energy for n = 1, 1.5, 2, and 5. The results predicted by the Bradley-n and JKR-n-G models are also plotted in dashed line for comparison. The critical Tabor number for the existence of hysteresis energy is 0.63.

and

$$-\bar{P}_c^{\text{JKR-}n\text{-G}} \equiv \frac{-P_c^{\text{JKR-}n\text{-G}}}{\pi Q^{2/n}\Delta\gamma z_0^{2/n-1}} = \frac{2^{4/n}n}{n+2}\mu^{(2-n)/n}, \tag{38}$$

respectively. The FSCM pull-off force approaches the corresponding Bradley limit at small Tabor numbers for each n. As the Tabor number increases, the FSCM pull-off force first approaches and then moves away from the JKR limit (except for the case of $n = 2$), which indicates that the JKR theory is no longer the soft limit for Gibson solid. This phenomenon is essentially different from the homogeneous and the power-law graded cases, which will be further discussed in Section 3.4.

3.3. Adhesion hysteresis and surface deformation mode

Following previous studies on adhesion between solids [32,55–57], this study does not consider the detailed dynamic process of jumping and the possible stored energy in this process, and thus the energy difference during a complete loading/unloading circle can be only regarded as the adhesion hysteresis in a quasi-static process, resulting in an apparent energy loss. The dependency of the apparent hysteresis energy loss ΔE on the Tabor number is studied for the cases of n = 1, 1.5, 2, and 5, as illustrated in Fig. 8(b). The apparent hysteresis energy is zero for small Tabor numbers. Only when the Tabor number is larger than the critical value μ_c, adhesion hysteresis occurs, and then the apparent hysteresis energy increases monotonously with the Tabor number. It is interesting to find that the critical value of the Tabor number is independent of the shape index. This indicates that the occurrence of the adhesion hysteresis (or jumping instability) of Gibson solid originates from its specific nature. The jumping-in condition is given by

$$\left(\frac{\mathrm{d}\bar{\delta}}{\mathrm{d}\bar{P}}\right)_B = \left(\frac{\mathrm{d}\bar{\delta}/\mathrm{d}\bar{H}_0}{\mathrm{d}\bar{P}/\mathrm{d}\bar{H}_0}\right)_B = 0, \tag{39}$$

where subscript B represents the jumping-in point. The value of $\mathrm{d}\bar{P}/\mathrm{d}\bar{H}_0$ at the jumping-in point is finite, and Eq. (39) is equivalent to $\left(\mathrm{d}\bar{\delta}/\mathrm{d}\bar{H}_0\right)_B = 0$. At the jumping point, the repulsive force is much smaller than the attractive force, and in Eq. (29), the ninth power term can safely be neglected by comparison with the third power term [14,55,56]. Consequently, Eq. (29) simplifies to

$$\bar{\delta} \sim -\bar{H}_0 - \frac{16}{3}\mu^2\left(\bar{H}_0 + 1\right)^{-3}. \tag{40}$$

By using the jumping-in condition $\left(\mathrm{d}\bar{\delta}/\mathrm{d}\bar{H}_0\right)_B = 0$, the surface central gap at the jumping-in point B is

$$\bar{H}_{0B} \sim 2\sqrt{\mu} - 1. \tag{41}$$

Substituting Eq. (41) into Eq. (40) yields the displacement at point B

$$\bar{\delta}_B \sim -\frac{8}{3}\sqrt{\mu} + 1. \tag{42}$$

This gives the asymptotic solution to the jumping-in position, which also indicates that the occurrence of the adhesion hysteresis (or jumping instability) of Gibson solid is independent of the surface shape and only depends on the Tabor number.

The effect of the Tabor number on the surface deformation is analyzed. The deformation corresponding to the pull-off point and zero-load point are given as representative cases in Fig. 9 for $n = 2$. For small Tabor numbers (e.g., μ = 0, 0.3, and 0.5), the surface deformation is single-valued and the folding deformation mode does not appear. With the increase of the Tabor number, the folding deformation starts to emerge and becomes apparent. The critical Tabor number for the appearance of folding deformation mode is identical to that for the appearance of adhesion hysteresis, i.e., $\mu_c \approx 0.63$.

3.4. Verification of the M–D-n-G and JKR-n-G models

The full self-consistent model can be applied to verify the existing adhesive contact models for Gibson solids. The JKR model on the adhesive contact between a sphere and a Gibson solid, namely the JKR-G model, was presented by Chen et al. [5]. The displacement and force predicted by the JKR-G model are given by

$$\delta = \frac{a^2}{2R} - \sqrt{\frac{3\Delta\gamma c_0}{E_0}}, \tag{43}$$

$$P = \frac{\pi E_0 a^4}{6Rc_0} - 2\pi a^2\sqrt{\frac{\Delta\gamma E_0}{3c_0}}, \tag{44}$$

respectively, where a is the contact radius. The M–D model on the adhesion between a power-law shaped intender and a Gibson solid, denoted as the M–D-n-G model, was developed by Jin et al. [10]. The displacement and force predicted by the M–D-n-G model are written as

$$\delta = \frac{a^n}{nQ} - \frac{3\sigma_0 c_0}{2E_0}, \tag{45}$$

$$P = \frac{2\pi E_0 a^{n+2}}{3Qc_0(n+2)} - \pi\sigma_0 c^2, \tag{46}$$

respectively, where σ_0 is the cohesive stress in the cohesive zone ($a < r < c$). Parameter c is determined from the Griffith relation

$$\frac{\sigma_0}{nQ}\left(c^n - a^n\right) + \frac{3c_0\sigma_0^2}{4E_0} = \Delta\gamma. \tag{47}$$

By introducing the following dimensionless parameters

$$\tilde{\delta} = \frac{\delta}{\left[3\Delta\gamma c_0/(4E_0)\right]^{1/2}},\quad \tilde{P} = \frac{P}{\pi\left[Q^4\Delta\gamma^{n+2}\left(3c_0/(4E_0)\right)^{2-n}\right]^{1/(2n)}},$$

$$\tilde{a} = \frac{a}{\left[3Q^2\Delta\gamma c_0/(4E_0)\right]^{1/(2n)}},\quad m = \frac{c}{a}, \tag{48}$$

the M–D-n-G solution can be rewritten as

$$\tilde{\delta} = \frac{\tilde{a}^n}{n} - 2\Lambda, \tag{49}$$

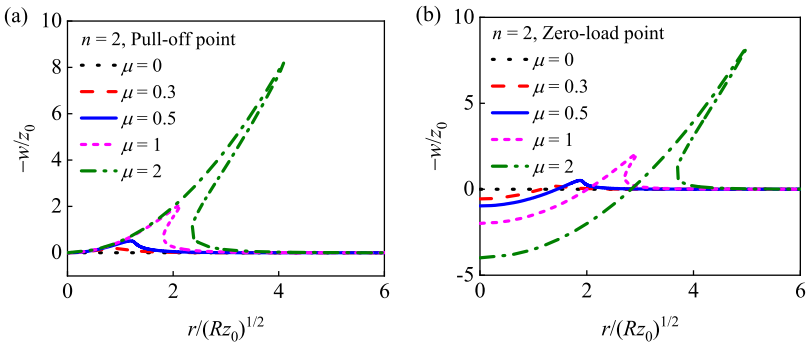

Fig. 9. Effect of the Tabor number μ on the surface deformation corresponding to (a) the pull-off point and (b) the zero-load point for $n = 2$. The representative values of μ are 0, 0.3, 0.5, 1, and 2. Folding deformation phenomenon appears for large Tabor numbers.

$$\tilde{P} = \frac{\tilde{a}^{n+2}}{2n+4} - \Lambda m^2 \tilde{a}^2, \tag{50}$$

$$m^n = \frac{n\left(1-\Lambda^2\right)}{\Lambda \tilde{a}^n} + 1, \tag{51}$$

where Λ is the Maugis number for Gibson solid, defined as

$$\Lambda = \frac{\sigma_0}{\sqrt{4E_0\Delta\gamma/\left(3c_0\right)}}. \tag{52}$$

The range of the Maugis number for homogeneous and power-law graded materials is 0 to ∞. But, for Gibson solid, Eq. (51) restricts Λ from 0 to 1 because c should be larger than a (i.e., $m \geq 1$) in the M–D-n-G model [10]. The M–D-n-G model reduces to the JKR-type model (denoted as the JKR-n-G model) when Λ approaches 1, i.e.,

$$\tilde{\delta} = \frac{\tilde{a}^n}{n} - 2, \tag{53}$$

$$\tilde{P} = \frac{\tilde{a}^{n+2}}{2n+4} - \tilde{a}^2, \tag{54}$$

and further reduces to the JKR-G model for $n = 2$ [10]. However, it can be found from Eq. (52) that the Maugis number for Gibson can be very large for soft materials (e.g., E_0 is very small). Therefore, the limitation of $\Lambda \leq 1$ is not physically reasonable.

The cohesive stress σ_0 should match a specific interaction such as the L–J law (Eq. (16)). Traditionally, σ_0 is chosen to equal to the theoretical stress of the L–J law [58–60]

$$\sigma_0 = \sigma_{\text{th}} \approx 1.026\frac{\Delta\gamma}{z_0}. \tag{55}$$

For convenience, Jin et al. [9,10] took $\sigma_0 \approx \Delta\gamma/z0$. Using this relation and combining with Eqs. (21) and (52) yield $\Lambda \approx \mu$. Hence, Jin et al. [9,10] did not distinguish these two dimensionless numbers. In fact, the value of the cohesive stress σ_0 may affect the prediction accuracy of the M–D-type models, and an improved strategy, namely *the rigid-limit-consistency condition*, has been proposed by Zheng and Yu [51] when studying the adhesion of homogeneous material with power-law surface shapes. The Zheng–Yu strategy determines the value of σ_0 by making the pull-off force of the DMT model and that of the Bradley model identical [51,61]. This strategy has been successfully applied to the adhesion of wavy surfaces [38] and power-law graded materials [14]. For convenience, the present study does not consider this effect and still adopts the traditional strategy to determine the value of σ_0. In the following discussion, the Maugis number and the Tabor number are not distinguished and are referred to as the Tabor number μ, as done by Jin et al. [10].

The force–displacement curves of the FSCM and the M–D-n-G model are compared for $n = 1.5$, 2 and 5 and $\mu = 0.5$ and 1, as shown in Fig. 10. For each case, the FSCM gives a full force–displacement curve and shows more details than the M–D-n-G model. For $n = 2$, the M–D-n-G model coincides well with FSCM at the high load branches, especially for the part near the pull-off point. For $n = 1.5$ and 5, an appreciable difference is observed between the two models, which implies that the adhesion results of non-paraboloidal punch are sensitive to the surface interaction. For $\mu = 1$, the force–displacement curves of the FSCM are bifurcated, while those of the M–D-n-G (JKR-n-G) model are single-valued. This indicates that the M–D-n-G and the JKR-n-G models cannot predict the jumping instability and adhesion hysteresis of Gibson solid.

The surface deformation and pressure distribution corresponding to the pull-off points of the FSCM and the M–D-n-G model are analyzed for $n = 2$ and $\mu = 0.5$ or 1, as shown in Fig. 11. For $\mu = 0.5$, the surface deformation and pressure distribution of the two models are both single-valued. For $\mu = 1$, the folding deformation mode is observed in the FSCM, but it cannot be detected by the M–D-n-G (JKR-n-G) model. It has been shown that the folding deformation and the jumping instability occur for the Gibson solid for $\mu \geq \mu_c \approx 0.63$. Hence, the M–D-$n$-G and the JKR-$n$-G models cannot predict the jumping instability because of their incorrect prediction of the surface deformation at large Tabor numbers. This proves that the restriction of the Tabor number in the M–D-n-G model stems from its inherent limitations on deformation. That is, the M–D-n-G model fails at large Tabor numbers because the contact and cohesive zones cannot be well defined due to the folding deformation.

The variation of the pull-off forces of the FSCM and the M–D-n-G model with the Tabor number is analyzed for $n = 1.5$, 2, and 5, as shown in Fig. 12. Note that the Tabor number in the M–D-n-G model is restricted to the range 0 to 1, while the FSCM does not have such constraint. The JKR-n-G pull-off force can be written as [10]

$$-\tilde{P}_c^{\text{JKR}} \equiv \frac{-P_c^{\text{JKR}}}{\pi\left[Q^4\Delta\gamma^{n+2}\left(3c_0/\left(4E_0\right)\right)^{2-n}\right]^{1/2n}} = \frac{n}{n+2}2^{4/n}, \tag{56}$$

which is also plotted in Fig. 12 for comparison. For $n = 2$, the pull-off forces of the two models are independent of the Tabor number and equal to the JKR-n-G pull-off force. For $n = 1.5$ and 5, the pull-off force of the M–D-n-G model is monotonous and approaches the JKR-n-G pull-off force with the increase of the Tabor number. The dimensionless pull-off force $-\tilde{P}_c$ of the FSCM as a function of μ has an extreme point (denoted as hollow dots), which is very close to the position of the JKR-n-G pull-off force (denoted as solid dots). The FSCM pull-off force first approaches and then departs from the JKR-n-G pull-off force with the increase of the Tabor number, which indicates that the JKR-type solution is no longer the soft limit for the adhesion of Gibson solid. By comparing with the FSCM, it can be found that the M–D-n-G model underestimates the pull-off force for $n = 1.5$ and overestimates the pull-off force for $n = 5$ when the Tabor number ranges from 0 to 1.

3.5. The soft limit for the adhesion of Gibson solid

It has been shown that the JKR-n-G pull-off force corresponding to $\mu = 1$ is not the soft limit for the adhesion of Gibson solid. Here, we determine the soft limit for the adhesion of Gibson with an asymptotic

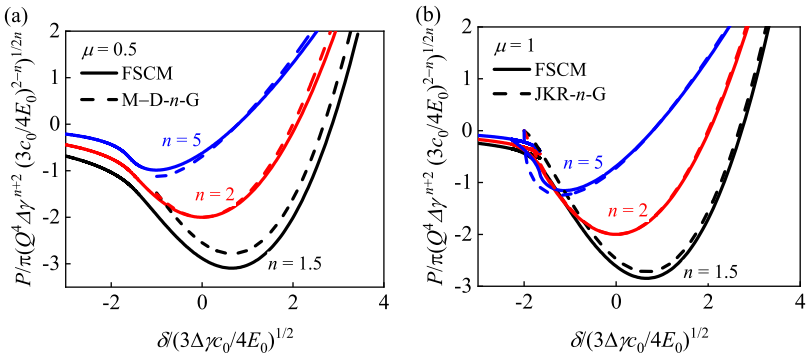

Fig. 10. Comparison of the force–displacement curves predicted by the FSCM (solid line) and the M–D-n-G model (dashed line) with different shape index. The Tabor number μ is 0.5 in (a) and 1 in (b). The M–D-n-G model reduces to the JKR-n-G model for $\mu = 1$.

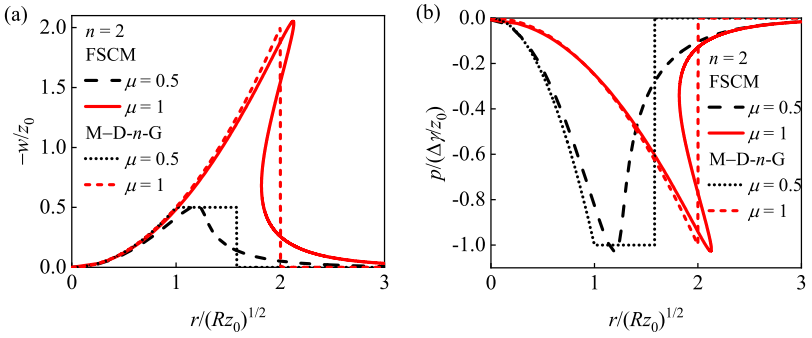

Fig. 11. Comparison of (a) the surface deformation and (b) the pressure distribution predicted by the FSCM and the M–D-n-G model for $n = 2$ and $\mu = 0.5$ and 1. The M–D-n-G model reduces to the JKR-n-G model for $\mu = 1$.

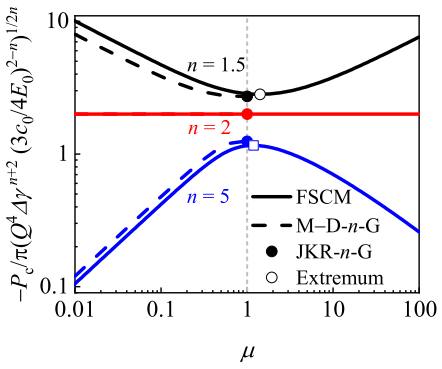

Fig. 12. Variation of the pull-off force with the Tabor number: comparison between the FSCM (solid line) and the M–D-n-G model (dashed line) for $n = 1.5$, 2, and 5. The extremum of the FSCM pull-off forces are plotted in hollow dots. The pull-off force of the JKR-n-G model corresponding to $\mu = 1$ is also plotted in solid dots for comparison.

analysis when considering $\mu \to \infty$. For simplicity, we take a new variable

$$\xi = \left(\bar{H} + 1\right)^{-3}, \tag{57}$$

and then Eqs. (29) and (30) can be rewritten as

$$\bar{\delta} = -\xi_0^{-1/3} + 1 + \frac{16}{3}\mu^2\left(\xi_0^3 - \xi_0\right), \tag{58}$$

$$\bar{P} = \int_{\bar{H}=\bar{H}_0}^{\bar{H}=\infty} \bar{p}_s(\bar{H})\, \mathrm{d}\bar{r}^2(\bar{H})$$

$$= \frac{8}{3}n^{2/n}\int_{\xi=\xi_0}^{\xi=0}\left(\xi^3 - \xi\right)\mathrm{d}\left[\bar{\delta} + \xi^{-1/3} - 1 - \frac{16}{3}\mu^2\left(\xi^3 - \xi\right)\right]^{2/n}, \tag{59}$$

where $\xi_0 = \left(\bar{H}_0 + 1\right)^{-3}$, which ranges from 0 to ∞. Through integration by parts, Eq. (59) yields

$$\bar{P} = \frac{8}{3}n^{2/n}\int_0^{\xi_0}\left[\bar{\delta} + \xi^{-1/3} - 1 - \frac{16}{3}\mu^2\left(\xi^3 - \xi\right)\right]^{2/n}\left(3\xi^2 - 1\right)\mathrm{d}\,\xi. \tag{60}$$

To facilitate asymptotic analysis, the characteristic of the numerical solutions of Eqs. (30) (or Eq. (60)) corresponding to the pull-off point for very large Tabor numbers is studied. The variations of $\bar{H}_{0c}$, ξ_{0c}, $\bar{\delta}_c/\mu^2$ and $-\bar{P}_c$ with μ are shown in Fig. 13, where subscript c represents the pull-off point. As $\mu \to \infty$, $\bar{H}_{0c}$ approaches zero and ξ_{0c} approaches 1, as shown in Figs. 13(a) and 13(b). Then, by applying Newton's binomial theorem, the pull-off force at the soft limit can be achieved by

$$\bar{P}_c^{\mathrm{soft}} \sim \frac{8}{3}n^{2/n}\int_0^1 \sum_{\alpha=0}^{\infty}\frac{(2/n)_\alpha}{\alpha!} \times \left[\bar{\delta}_c - 1 - \frac{16}{3}\mu^2\left(\xi^3 - \xi\right)\right]^{2/n-\alpha}\left(\xi^{-1/3}\right)^\alpha\left(3\xi^2 - 1\right)\mathrm{d}\,\xi, \tag{61}$$

where $(\cdot)_\alpha$ is the falling factorial, e.g., $(2/n)_\alpha = (2/n)(2/n-1)\cdots(2/n-\alpha+1)$ and $(2/n)_0 = 1$. Note that as $\mu \to \infty$, $\left(\bar{\delta}_c - 1\right)/\mu^2 \to 0$ (Fig. 13(c)) and the expansions can retain only high-order terms with respect to μ, e.g., the first two terms. As a result, Eq. (61) follows an asymmetric behavior

$$\bar{P}_c^{\mathrm{soft}} \sim \bar{P}_0 + \bar{P}_1, \tag{62}$$

where $\bar{P}_0$ and $\bar{P}_1$ are given by

$$\bar{P}_0 = \frac{8}{3}n^{2/n}\int_0^1\left[-\frac{16}{3}\mu^2\left(\xi^3 - \xi\right)\right]^{2/n}\left(3\xi^2 - 1\right)\mathrm{d}\,\xi, \tag{63}$$

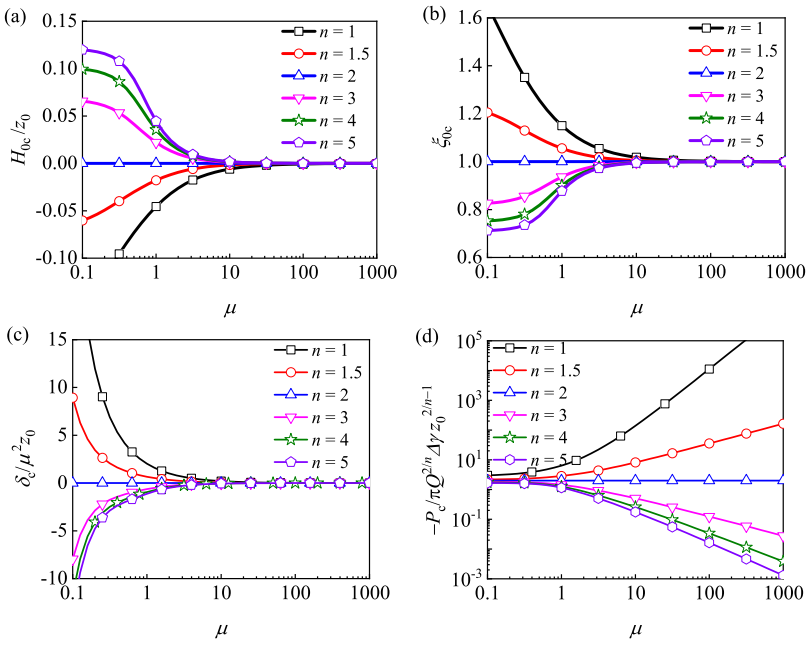

Fig. 13. Effect of the Tabor number μ on the numerical solutions at the pull-off point: (a) $\bar{H}_{0c}$, (b) ξ_{0c}, (c) $\bar{\delta}_c/\mu^2$, and (d) $-\bar{P}_c$. The representative values of the shape index n are 1, 1.5, 2, 3, 4, and 5. As $\mu \to \infty$, we have $\bar{H}_{0c} \to 0$, $\xi_{0c} \to 1$, $\bar{\delta}_c/\mu^2 \to 0$ for all values of n.

$$\bar{P}_1 = \frac{8}{3}n^{2/n}\int_0^1 \frac{2}{n}\left[-\frac{16}{3}\mu^2\left(\xi^3-\xi\right)\right]^{2/n-1}\left(\xi^{-1/3}\right)\left(3\xi^2-1\right)\mathrm{d}\,\xi. \tag{64}$$

It is found that

$$\bar{P}_0 = \frac{8}{3}n^{2/n}\int_{\xi=0}^{\xi=1}\left[-\frac{16}{3}\mu^2\left(\xi^3-\xi\right)\right]^{2/n}\mathrm{d}\left(\xi^3-\xi\right) = 0, \tag{65}$$

because the integrand is bounded in the integral domain and the term $\xi^3 - \xi$ equals 0 at the upper and lower integral limit. Therefore, $\bar{P}_1$ becomes the primary term of $\bar{P}_c^{\mathrm{soft}}$, written as

$$\bar{P}_c^{\mathrm{soft}} \sim \bar{P}_1 = \left(\frac{16}{3}\right)^{2/n} n^{2/n-1}\mu^{2(2-n)/n}\int_0^1 \left(\xi-\xi^3\right)^{2/n-1}\left(\xi^{-1/3}\right)\left(3\xi^2-1\right)\mathrm{d}\,\xi. \tag{66}$$

Hence, an asymptotic solution of the pull-off force for the soft limit is given by

$$-\bar{P}_c^{\mathrm{soft}} \sim \frac{(16n/3)^{2/n}}{6-n}\mathrm{B}\left(5/6+1/n, 2/n\right)\mu^{2(2-n)/n}, \quad 0<n<6. \tag{67}$$

The integral in Eq. (66) converges only for $0 < n < 6$, so the efficient range of the asymptotic solution is $0 < n < 6$. For very large n, the surface shape of the intender is relatively flat in the center region and becomes extremely sharp at the edge [60]. In practical applications, such as atomic force microscopy (AFM), this kind of surface shape is rare and the case of $n \le 5$ is enough for actual implementation [60]. Our asymptotic solution (Eq. (67)) predicts a different power-law $\bar{P}_c$–μ relation from that of the JKR-n-G model (Eq. (38)). The exponent on the Tabor number in the asymptotic solution is twice that of the JKR-n-G theory.

The pull-off force is scaled in a new format, i.e., $-\bar{P}_c/\mu^{2(2-n)/n}$, to verify the accuracy of the asymptotic solution. The variation of $-\bar{P}_c/\mu^{2(2-n)/n}$ with μ obtained from Eq. (30) using numerical integration is shown in Fig. 14, and the soft limit predicted by Eq. (67) is also plotted for comparison. The dimensionless pull-off force approaches constant values for large Tabor numbers, indicating that our asymptotic relation, i.e., $-\bar{P}_c = O(\mu^{2(2-n)/n})$, is valid for $\mu \to \infty$. For the cases of $n \le 4$ considered, it is obvious that these constant values can be predicted by Eq. (67). But for the case of $n = 5$, the approaching rate of the numerical results to the soft limit is quite slow and there is a considerable deviation between the numerical and asymptotic results

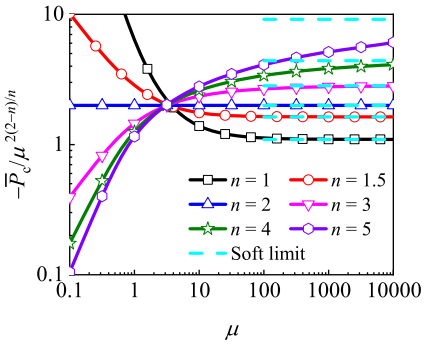

Fig. 14. Variation of the pull-off force with the Tabor number μ. The exact solution is plotted in solid lines with symbols, and the soft limit predicted by the asymptotic solution is plotted in dashed lines. The representative values of the shape index n are 1, 1.5, 2, 3, 4, and 5.

even at extremely large Tabor numbers (say 10^4). Actually, for quite large Tabor numbers, it may be only of theoretical interest related to the present model, because the deformation of the material is so large and its mechanical response is beyond the scope of linear elasticity theory. Some other factors related to deformation suppression, such as friction [62–65] and surface tension [66–73], also need to be considered in the adhesive contact models. These questions remain open and await further studies.

4. Conclusions

The adhesive contact problem between an axisymmetric rigid power-law shaped punch and Gibson solid was revisited and a full self-consistent model (FSCM) was developed. The self-consistent relation for the adhesion of Gibson solid is an algebraic equation, and it can be explicitly solved by taking the surface gap as the independent variable. Therefore, the FSCM for the adhesion of Gibson solid provides the first explicit form of a self-consistent relation.

The force–displacement curve is bifurcated with an unstable jumping-in position over a critical Tabor number ($\mu \approx 0.63$), causing

adhesion hysteresis during a complete loading–unloading cycle. A folding deformation mode that the surface is flipped and folded along the radial direction is observed over this critical Tabor number. Compared with the FSCM, the M-D-*n*-G model [10] is invalid for large Tabor numbers, unable to predict the jumping instability and the adhesion hysteresis, because the contact and cohesive zones cannot be well defined due to the folding deformation. This also explains an interesting result that the JKR-type model [5,10,26], previously thought to be the soft limit of solid adhesion, is not the case for Gibson solid. The soft limit of the Gibson solid adhesion is obtained through numerical and asymptotic analysis using the FSCM.

Many interesting problems, such as the settlement of foundations on soils and the flaw-tolerant adhesion, have been explored by taking Gibson solid as a typical graded material in the literature [13,24,25]. We further established a self-consistent toy model for the adhesive contact of Gibson solid, and found that a folding deformation mode appears at large Tabor numbers and the JKR-type solution is not the soft limit for the adhesion of Gibson solid. These findings may be helpful for understanding the adhesion behavior of general graded materials, and indicate that the classical adhesive contact models may need some improvements to predict the folding deformation for both homogeneous and graded materials.

CRediT authorship contribution statement

Yudong Zhu: Investigation, Methodology, Software, Validation, Formal analysis, Writing – original draft. **Zhijun Zheng:** Conceptualization, Methodology, Formal analysis, Supervision, Writing – review & editing, Funding acquisition, Data curation, Project administration. **Chenguang Huang:** Supervision, Writing – review & editing. **Jilin Yu:** Supervision, Writing – review & editing.

Declaration of competing interest

The authors declare that they have no known competing financial interests or personal relationships that could have appeared to influence the work reported in this paper.

Data availability

Data will be made available on request.

Acknowledgments

This work is supported by the National Natural Science Foundation of China (Project No. 12272375).

References

[1] Peisker H, Michels J, Gorb SN. Evidence for a material gradient in the adhesive tarsal setae of the ladybird beetle Coccinella septempunctata. Nature Commun 2013;4:1661. http://dx.doi.org/10.1038/ncomms2576.

[2] Flenner S, Schaber CF, Krasnov I, Stieglitz H, Rosenthal M, Burghammer M, et al. Multiple mechanical gradients are responsible for the strong adhesion of spider attachment hair. Adv Mater 2020;32(37):2002758. http://dx.doi.org/10.1002/adma.202002758.

[3] Dong X, Zhang R, Tian Y, Ramos MA, Hu TS, Wang Z, et al. Functionally graded gecko setae and the biomimics with robust adhesion and durability. ACS Appl Polym Mater 2020;2:2658–66. http://dx.doi.org/10.1021/acsapm.0c00282.

[4] Chen S, Yan C, Soh A. Adhesive behavior of two-dimensional power-law graded materials. Int J Solids Struct 2009;46:3398–404. http://dx.doi.org/10.1016/j.ijsolstr.2009.05.006.

[5] Chen S, Yan C, Zhang P, Gao H. Mechanics of adhesive contact on a power-law graded elastic half-space. J Mech Phys Solids 2009;57:1437–48. http://dx.doi.org/10.1016/j.jmps.2009.06.006.

[6] Jin F, Guo X. Non-slipping adhesive contact of a rigid cylinder on an elastic power-law graded half-space. Int J Solids Struct 2010;47:1508–21. http://dx.doi.org/10.1016/j.ijsolstr.2010.02.010.

[7] Jin F, Guo X. Mode-mixity-dependent adhesion of power-law graded elastic solids under normal and substrate stretch-induced mismatch strain. Int J Solids Struct 2012;49:2349–57. http://dx.doi.org/10.1016/j.ijsolstr.2012.05.003.

[8] Jin F, Guo X. Mechanics of axisymmetric adhesive contact of rough surfaces involving power-law graded materials. Int J Solids Struct 2013;50:3375–86. http://dx.doi.org/10.1016/j.ijsolstr.2013.06.007.

[9] Jin F, Guo X, Gao H. Adhesive contact on power-law graded elastic solids: The JKR–DMT transition using a double-Hertz model. J Mech Phys Solids 2013;61:2473–92. http://dx.doi.org/10.1016/j.jmps.2013.07.015.

[10] Jin F, Tang Q, Guo X, Gao H. A generalized Maugis-Dugdale solution for adhesion of power-law graded elastic materials. J Mech Phys Solids 2021;154:104509. http://dx.doi.org/10.1016/j.jmps.2021.104509.

[11] Heß M. A simple method for solving adhesive and non-adhesive axisymmetric contact problems of elastically graded materials. Internat J Engrg Sci 2016;104:20–33. http://dx.doi.org/10.1016/j.ijengsci.2016.04.009.

[12] Willert E. Dugdale–Maugis adhesive normal contact of axisymmetric power-law graded elastic bodies. Facta Univers Ser Mech Eng 2018;16:9–18. http://dx.doi.org/10.22190/FUME171121003W.

[13] Gibson RE. Some results concerning displacements and stresses in a non-homogeneous elastic half-space. Geotechnique 1967;17:58–67. http://dx.doi.org/10.1680/geot.1967.17.1.58.

[14] Zhu YD, Zheng ZJ, Huang CG, Yu JL. Adhesion of graded elastic materials: A full self-consistent model and its application. J Mech Phys Solids 2022;169:105078. http://dx.doi.org/10.1016/j.jmps.2022.105078.

[15] Gibson RE, Kalsi GS. The surface settlement of a linearly inhomogeneous cross-anisotropic elastic half-space. ZAMP 1974;25:843–7. http://dx.doi.org/10.1007/BF01590269.

[16] Gibson RE, Sills GC. Settlement of a trip load on a non-homogeneous orthotropic incompressible elastic half-space. Quart J Mech Appl Math 1975;28:233–43. http://dx.doi.org/10.1093/qjmam/28.2.233.

[17] Gibson RE, Brown PT, Andrew KRF. Some results concerning displacements in a non-homogeneous elastic layer. ZAMP 1971;22:855–64. http://dx.doi.org/10.1007/BF01591813.

[18] Awojobi AO, Gibson RE. Plane strain and axially symmetric problems of a linearly nonhomogeneous elastic half-space. Q J Mech Appl Math 1973;26:285–302. http://dx.doi.org/10.1093/qjmam/26.3.285.

[19] Calladine CR, Greenwood JA. Line and point loads on a non-homogeneous incompressible elastic half-space. Q J Mech Appl Math 1978;31:507–29. http://dx.doi.org/10.1093/qjmam/31.4.507.

[20] Booker JR, Balaam NP, Davis EH. The behaviour of an elastic non-homogeneous half-space. Part I–Line and point loads. Int J Numer Anal Methods Geomech 1985;9:353–67. http://dx.doi.org/10.1002/nag.1610090405.

[21] Booker JR, Balaam NP, Davis EH. The behaviour of an elastic non-homogeneous half-space. Part II–Circular and strip footings. Int J Numer Anal Methods Geomech 1985;9:369–81. http://dx.doi.org/10.1002/nag.1610090406.

[22] Giannakopoulos AE, Suresh S. Indentation of solids with gradients in elastic properties: Part, I. Point force. Int J Solids Struct 1997;34:2357–92. http://dx.doi.org/10.1016/S0020-7683(96)00171-0.

[23] Giannakopoulos AE, Suresh S. Indentation of solids with gradients in elastic properties: Part, I.I. Axisymmetric indenters. Int J Solids Struct 1997;34:2393–428. http://dx.doi.org/10.1016/S0020-7683(96)00172-2.

[24] Yao H, Gao H. Mechanical principles of robust and releasable adhesion of gecko. J Adhes Sci Tech 2007;21:1185–212. http://dx.doi.org/10.1163/156856107782328326.

[25] Yao H, Gao H. Gibson-soil-like materials achieve flaw-tolerant adhesion. J Comput Theor Nanos 2010;7:1299–305. http://dx.doi.org/10.1166/jctn.2010.1484.

[26] Johnson KL, Kendall K, Roberts AD. Surface energy and contact of elastic solids. Proc R Soc Lond A 1971;324:301–13. http://dx.doi.org/10.1098/rspa.1971.0141.

[27] Greenwood JA, Johnson KL. An alternative to the Maugis model of adhesion between elastic spheres. J Phys D: Appl Phys 1998;31:3279–90. http://dx.doi.org/10.1088/0022-3727/31/22/017.

[28] Derjaguin BV, Muller VM, Toporov YP. Effect of contact deformations on the adhesion of particles. J Colloid Interface Sci 1975;53:314–26. http://dx.doi.org/10.1016/0079-6816(94)90044-2.

[29] Hughes BD, White LR. 'Soft' contact problems in linear elasticity. Q J Mech Appl Math 1979;32:445–71. http://dx.doi.org/10.1093/qjmam/32.4.445.

[30] Hughes BD, White LR. Implications of elastic deformation on the direct measurement of surface forces. JCS Faraday I 1980;76:963–78. http://dx.doi.org/10.1039/f19807600963.

[31] Muller VM, Yushchenko VS, Derjaguin BV. On the influence of molecular forces on the deformation of an elastic sphere and its sticking to a rigid plane. J Colloid Interface Sci 1980;77:91–101. http://dx.doi.org/10.1016/0021-9797(80)90419-1.

[32] Greenwood JA. Adhesion of elastic spheres. Proc R Soc Lond Ser A Math Phys Eng Sci 1997;453:1277–97. http://dx.doi.org/10.1098/rspa.1997.0070.

[33] Feng JQ. Contact behavior of spherical elastic particles: a computational study of particle adhesion and deformations. Colloids Surf A 2000;172:175–98. http://dx.doi.org/10.1016/S0927-7757(00)00580-X.

[34] Feng JQ. Adhesive contact of elastically deformable spheres: a computational study of pull-off force and contact radius. J Colloid Interface Sci 2001;238:318–23. http://dx.doi.org/10.1006/jcis.2001.7532.
[35] Zheng ZJ, Yu JL, Lin J, Li JR. Adhesive contact of power-law axisymmetric elastic objects. J Univ Sci Tech CHN 2007;37:1293–9 [in Chinese].
[36] Wu JJ. Adhesive contact between a cylinder and a half-space. J Phys D: Appl Phys 2009;42:155302. http://dx.doi.org/10.1088/0022-3727/42/15/155302.
[37] Wu JJ, Lin YJ. Numerical analyses on the adhesive contact between a sphere and a longitudinal wavy surface. J Adhesion 2015;91:381–408. http://dx.doi.org/10.1080/00218464.2014.914928.
[38] Zhu YD, Zheng ZJ, Zhang YL, Wu HA, Yu JL. Adhesion of elastic wavy surfaces: Interface strengthening/weakening and mode transition mechanisms. J Mech Phys Solids 2021;151:104402. http://dx.doi.org/10.1016/j.jmps.2021.104402.
[39] Derjaguin BV. Theorie des Anhaftens kleiner Teilchen (Theory of adhering small particles). Koll Z 1934;69:155–64. http://dx.doi.org/10.1016/0079-6816(92)90027-F.
[40] Greenwood JA. On the DMT theory. Tribol Lett 2007;26:203–11. http://dx.doi.org/10.1007/s11249-006-9184-7.
[41] Greenwood JA. Adhesion of small spheres. Phil Mag 2009;89:945–65. http://dx.doi.org/10.1080/14786430902832765.
[42] Rostovtsev NA. On certain solutions of an integral equation of the theory of a linearly deformable foundation. J Appl Math Mech 1964;28:127–45. http://dx.doi.org/10.1016/0021-8928(64)90137-6.
[43] Fabrikant VI, Sankar TS. On contact problems in an inhomogeneous half-space. Int J Solids Struct 1984;20:159–66. http://dx.doi.org/10.1016/0020-7683(84)90006-4.
[44] Lee D, Barber JR, Thouless MD. Indentation of an elastic half space with material properties varying with depth. Internat J Engrg Sci 2009;47:1274–83. http://dx.doi.org/10.1016/j.ijengsci.2008.08.005.
[45] Li Q, Popov VL. Boundary element method for normal non-adhesive and adhesive contacts of power-law graded elastic materials. Comput Mech 2018;61:319–29. http://dx.doi.org/10.1007/s00466-017-1461-9.
[46] Lyashenko IA, Popov VL. Contact properties of gradient materials with a high gradient index. Tech Phys 2022;67:28–33. http://dx.doi.org/10.1134/S1063784222010108.
[47] Lyashenko IA, Popov VL. Adhesion between a rigid indenter and an elastic half-space for incompressible gradient media with a high gradientness index. Tech Phys 2020;65:728–36. http://dx.doi.org/10.1134/S1063784220050151.
[48] Giannakopoulos AE, Pallot P. Two-dimensional contact analysis of elastic graded materials. J Mech Phys Solids 2000;48:1597–631. http://dx.doi.org/10.1016/S0022-5096(99)00068-X.
[49] Kassir MK, Chuaprasert MF. A rigid punch in contact with a nonhomogeneous elastic solid. J Appl Mech 1974;41:1019–24. http://dx.doi.org/10.1115/1.3423426.
[50] Argatov II, Sabina FJ. Recovery of information on the depth-dependent profile of elastic FGMs from indentation experiments. Internat J Engrg Sci 2022;176:103659. http://dx.doi.org/10.1016/j.ijengsci.2022.103659.
[51] Zheng ZJ, Yu JL. Using the dugdale approximation to match a specific interaction in the adhesive contact of elastic objects. J Colloid Interface Sci 2007;310:27–34. http://dx.doi.org/10.1016/j.jcis.2007.01.042.
[52] Van Limbeek MAJ, Essink MH, Pandey A, Snoeijer JH, Karpitschka S. Pinning-induced folding-unfolding asymmetry in adhesive creases. Phys Rev Lett 2021;127:028001. http://dx.doi.org/10.1103/physrevlett.127.028001.
[53] Oshri O, Liu Y, Aizenberg J, Balazs AC. Delamination of a thin sheet from a soft adhesive Winkler substrate. Phys Rev E 2018;97:062803. http://dx.doi.org/10.1103/physreve.97.062803.
[54] Twohig T, Croll AB. Adhesion directed capillary origami. Soft Matter 2021;17:9170–80. http://dx.doi.org/10.1039/d1sm01142a.
[55] Wu JJ. The jump-to-contact distance in atomic force microscopy measurement. J Adhes 2010;86:1071–85. http://dx.doi.org/10.1080/00218464.2010.519256.
[56] Ciavarella M, Greenwood JA, Barber JR. Effect of Tabor parameter on hysteresis losses during adhesive contact. J Mech Phys Solids 2017;98:236–44. http://dx.doi.org/10.1016/j.jmps.2016.10.005.
[57] Ciavarella M, Joe J, Papangelo A, Barber JR. The role of adhesion in contact mechanics. J R Soc Interface 2019;16:20180738. http://dx.doi.org/10.1098/rsif.2018.0738.
[58] Maugis D. Adhesion of spheres: the JKR–DMT transition using a Dugdale model. J Colloid Interface Sci 1992;150:243–69. http://dx.doi.org/10.1016/0021-9797(92)90285-T.
[59] Johnson KL, Greenwood JA. Maugis analysis of adhesive line contact. J Phys D: Appl Phys 2008;41:155315. http://dx.doi.org/10.1088/0022-3727/41/15/155315.
[60] Grierson DS, Liu J, Carpick RW, Turner KT. Adhesion of nanoscale asperities with power-law profiles. J Mech Phys Solids 2013;61(2):597–610. http://dx.doi.org/10.1016/j.jmps.2012.09.003.
[61] Zheng ZJ, Yu JL. A generalized maugis model for adhesive contact of arbitrary axisymmetric elastic objects. Lixue Xuebao/Chin J Theoret Appl Mech 2007;39(3):382–8 [in Chinese].
[62] Stingl B, Ciavarella M, Hoffmann N. Frictional dissipation in elastically dissimilar oscillating Hertzian contacts. Int J Mech Sci 2013;72:55–62. http://dx.doi.org/10.1016/j.ijmecsci.2013.03.012.
[63] Bazrafshan M, de Rooij MB, Schipper DJ. The effect of adhesion and roughness on friction hysteresis loops. Int J Mech Sci 2019;155:9–18. http://dx.doi.org/10.1016/j.ijmecsci.2019.02.027.
[64] Menga N, Carbone G, Dini D. Exploring the effect of geometric coupling on friction and energy dissipation in rough contacts of elastic and viscoelastic coatings. J Mech Phys Solids 2021;148:104273. http://dx.doi.org/10.1016/j.jmps.2020.104273.
[65] Carbone G, Mandriota C, Menga N. Theory of viscoelastic adhesion and friction. Extreme Mech Lett 2022;56:101877. http://dx.doi.org/10.1016/j.eml.2022.101877.
[66] Long JM, Wang GF, Feng XQ, Yu SW. Two-dimensional Hertzian contact problem with surface tension. Int J Solids Struct 2012;49:1588–94. http://dx.doi.org/10.1016/j.ijsolstr.2012.03.017.
[67] Long JM, Wang GF. Effects of surface tension on axisymmetric Hertzian contact problem. Mech Mater 2013;56:65–70. http://dx.doi.org/10.1016/j.mechmat.2012.09.003.
[68] Long JM, Wang GF, Feng XQ, Yu SW. Effects of surface tension on the adhesive contact between a hard sphere and a soft substrate. Int J Solids Struct 2016;84:133–8. http://dx.doi.org/10.1016/j.ijsolstr.2016.01.021.
[69] Vasu TS, Bhandakkar TK. Plane strain cylindrical indentation of functionally graded half-plane with exponentially varying shear modulus in the presence of residual surface tension. Int J Mech Sci 2018;135:158–67. http://dx.doi.org/10.1016/j.ijmecsci.2017.11.009.
[70] Zhu XY, Xu W. Effect of surface tension on the behavior of adhesive contact based on Lennard-Jones potential law. J Mech Phys Solids 2018;111:170–83. http://dx.doi.org/10.1016/j.jmps.2017.11.001.
[71] Zhu XY, Zhai JH, Xu W. Analysis of surface-loaded problem of nonhomogeneous elastic half-plane with surface tension. Mech Mater 2019;129:254–64. http://dx.doi.org/10.1016/j.mechmat.2018.11.008.
[72] Zhu XY, Xu W, Qin YD. Effect of surface tension on the behavior of adhesive contact based on Maugis–Dugdale model. Eur J Mech A-Solid 2020;81:103930. http://dx.doi.org/10.1016/j.euromechsol.2019.103930.
[73] Zhu XY, Wang SW, Qin R. The effect of surface tension on the adhesion performance of nanoscale fibrillary structures–a theoretical prediction. Eur J Mech A-Solid 2022;96:104746. http://dx.doi.org/10.1016/j.euromechsol.2022.104746.